## 3D zoning of barium in alkali feldspar

## JORDAN LUBBERS<sup>1,\*</sup>, ADAM KENT<sup>1</sup>, DOUGLAS MEISENHEIMER<sup>2</sup>, AND DORTHE WILDENSCHILD<sup>2</sup>

<sup>1</sup>College of Earth, Ocean, and Atmospheric Sciences, Oregon State University, Corvallis, Oregon 97331, U.S.A. 
<sup>2</sup>College of Engineering, Oregon State University, Corvallis, Oregon, 97331, U.S.A.

#### ABSTRACT

Interpretation of chemical zoning within igneous minerals is critical to many petrologic studies. Zoning in minerals, however, is commonly observed in thin sections or grain mounts, which are random 2D slices of a 3D system. Use of these 2D sections to infer 3D geometries requires a set of assumptions, often not directly tested, introduces several issues, and results in partial loss of zoning information. Computed X-ray microtomography (microCT) offers a way to assess 3D zoning in minerals at high resolution. To observe 3D mineral zoning using microCT, however, requires that zoning is observable as differences in X-ray attenuation. Sanidine, with its affinity for Ba in the crystal lattice, can display large, abrupt variations in Ba that are related to various magma reservoir processes. These changes in Ba also significantly change the X-ray attenuation coefficient of sanidine, allowing for discrete mineral zones to be mapped in 3D using microCT. Here we utilize microCT to show 3D chemical zoning within natural sanidines from a suite of volcanic eruptions throughout the geologic record. We also show that changes in microCT grayscale in sanidine are largely controlled by changes in Ba. Starting with 3D mineral reconstructions, we simulate thin-section making by generating random 2D slices across a mineral zone to show that slicing orientation alone can drastically change the apparent width and slope of composition transitions between different zones. Furthermore, we find that chemical zoning in sanidine can commonly occur in more complex geometries than the commonly interpreted concentric zoning patterns. Together, these findings have important implications for methodologies that rely on the interpretation of chemical zoning within minerals and align with previously published numerical models that show how chemical gradient geometries are affected by random sectioning during common sample preparation methods (e.g., thin sections and round mounts).

**Keywords:** Computed X-ray microtomography, mineral zoning, sanidine, barium

## Introduction

Chemical zoning is nearly ubiquitous in igneous minerals, and the compositions of zoned crystals preserve records of magmatic conditions and compositions when mineral growth occurred. Therefore, documenting and interpreting such zoning, as well as relating compositional variations to textural features, is a crucial pillar upon which modern igneous petrology is based. Studies of mineral chemical zoning provide important insights into common igneous processes such as magma mixing (e.g., Streck et al. 2005; Kent et al. 2010; Eichelberger 1975; Anderson 1976; Simonetti et al. 1996); frequency and origins of magma recharge (e.g., Tepley et al. 2000; Davidson et al. 2001; Davidson and Tepley 1997; Singer et al. 1995); thermal evolution of magma reservoirs (e.g., Cooper and Kent 2014; Rubin et al. 2017; Shamloo and Till 2019); and the rates of igneous processes (e.g., Costa and Dungan 2005; Ruprecht and Plank 2013; Costa et al. 2003; Morgan and Blake 2006). Changes in mineral chemistry can also be used to understand the temporal sequence and evolution of these and other processes (Cooper 2017). When applied to a sufficiently large and representative population of grains, this approach then allows the long-term physicochemical conditions within a given magmatic system to be constrained.

Many mineral zoning studies, however, only investigate the interplay between chemical zoning and mineral textures using 2D exposures (i.e., thin sections or mineral mounts). However, use of 2D mineral zoning patterns to represent 3D systems can also introduce several artifacts and other issues (e.g., incorrect estimates of mineral size and shape, width of compositional zones, modification of compositional gradients, etc.), potentially leading to incomplete and or inaccurate characterization and interpretation of igneous processes (e.g., Higgins 2000). For example, recent studies have numerically investigated the effects of sectioning 3D zoned crystals using modeling approaches for the purposes of documenting diffusion gradients (e.g., Shea et al. 2015; Krimer and Costa 2017; Couperthwaite et al. 2021). This shows that many 2D sections suffer from partial loss of zoning information, requiring a careful evaluation of each crystal studied to avoid a distorted view of the true concentration gradient between chemical zones and obtain reliable results (e.g., diffusion timescales). Despite this realization, however, studies of 3D zoning in natural mineral examples have been relatively underutilized to address 2D sectioning issues.

To observe natural mineral chemical zoning in 3D, previous studies have used serial sectioning combined with either electron probe (e.g., Spear and Daniel 2003), focused ion beam time of flight secondary ion mass spectrometry (FIB ToF SIMS) (Wirth

<sup>\*</sup> E-mail: jelubber@gmail.com. Orcid 0000-0002-3566-5091

2009; Tajčmanová et al. 2012), or atom probe tomography (APT) (Reddy et al. 2020; Rickard et al. 2020), however these approaches: (1) often only produce 3D imaging/chemical information for an extremely small volume and are difficult to apply to an entire mineral (e.g., FIB ToF SIMS, APT); (2) can only create coarse 3D reconstructions based on limited 2D slices (electron probe serial sections); (3) necessitate the destruction of the sample being studied; and (4) are extremely time consuming making it challenging to be representative of an entire magmatic system.

In recent years, technological developments in high-resolution imaging via absorption (e.g., Uesugi et al. 2010; Tsuchiyama et al. 2013; Pankhurst et al. 2018; Mourey and Shea 2019) and phase contrast (e.g., Arzilli et al. 2015, 2016) computed X-ray microtomography (microCT) have provided new opportunities to observe textural and zoning characteristics throughout individual minerals in 3D. These studies show there is great potential to further use microCT and related techniques [e.g., Diffraction Contrast Tomography; Pankhurst et al. (2019)] to document and understand compositional zoning in igneous minerals, but there remains a need to develop a greater understanding of the potential for using microCT in different mineral systems, and to establish what the 3D variations in X-ray attenuation revealed by microCT correspond to in terms of compositional variations for specific minerals. In this study, we use absorption microCT to document intracrystalline 3D chemical zoning of natural sanidine crystals and explore the geochemical controls responsible for changes in X-ray attenuation throughout this mineral.

## X-RAY MICROTOMOGRAPHY

When X-rays interact with a sample, they are attenuated according to Lambert-Beer's Law:

$$I = I_0 \exp(-\mu D) \tag{1}$$

where I is the attenuated intensity of X-rays after they pass through a sample of thickness D,  $I_0$  is the incident radiation (X-ray) intensity, and  $\mu$  is the linear attenuation coefficient of the material the X-rays are interacting with. The linear attenuation coefficient is a constant that describes the fraction of attenuated incident photons in a monoenergetic beam per unit thickness of a material and varies with beam energy, atomic electron density, and the bulk density of the material (Wildenschild and Sheppard 2013). Although attenuation mechanisms also vary with beam energy (i.e., Compton scattering for  $5 < I_0 < 10$  MeV; pair production  $I_0 > 10$  MeV), for geologic materials, a beam energy of 50-100 keV is typically used and the photoelectric effect dominates (Mccullough 1975). This is an extremely useful observation as both the photoelectric effect and Compton scattering are sensitive to the atomic number of an element (Van Grieken and Markowicz 2002), allowing for the possibility of correlating changes in linear attenuation coefficient to changes in chemical composition of minerals and other geologic materials. Earlier attempts to use absorption contrast microCT to quantify intracrystalline chemical heterogeneity within olivine and pyroxene from meteorites were successfully made by Uesugi et al. (2010) and Tsuchiyama et al. (2013), respectively; however, attempts to apply this methodology to terrestrial igneous minerals have been underutilized (Pankhurst et al. 2014, 2018) and largely aimed at textural analysis (e.g., Pamukcu and Gualda 2010; Zandomeneghi et al. 2010; Giachetti et al. 2011; Voltolini et al. 2011). Phase contrast tomography has also been utilized on geologic materials to help distinguish between similarly attenuating phases (i.e., feldspar and matrix glass; Arzilli et al. 2016) by improving signal-to-noise ratios; however, it is important to note that grayscale images produced from the reconstruction using this method contain values that do not correlate directly with linear attenuation coefficients (Boone et al. 2012). As we are concerned with not only observing chemical zoning in 3D, but understanding which elements are largely responsible for controlling X-ray attenuation in sanidine (e.g., those that change the linear attenuation coefficient significantly), we have not explored phase-contrast tomography in this study. Furthermore, our image segmentation pipeline (see Image Processing section below) has been successful at increasing signal-to-noise ratios within our data to sufficiently allow for the accurate segmentation of unique phases (i.e., feldspar, glass, epoxy). Thorough reviews further expanding on previous applications of X-ray computed tomography within the geosciences can be found in Hanna and Ketcham (2017) as well as Cnudde and Boone (2013). For a more comprehensive description of photon interaction with matter, the reader is referred to Mccullough (1975) and Van Grieken and Markowicz (2002).

To create tomographic images of a material, X-rays must pass through the sample from many directions and then be combined through reconstruction methods to produce a stack of 2D "slices." A slice is compiled from X-ray intensity measurements at a given height for a full 360° rotation around the sample and, when monochromatic X-ray beams are used, can be thought of as a spatial distribution of linear attenuation coefficient (µ) values (Denison et al. 1997). Each slice represents a finite thickness based on setup conditions, and these slices can then be further combined to construct a 3D rendering of the sample that can then be quantitatively investigated. Although there are a few types of scanning in commercial microCT setups, the method used in this study employs helical scanning from a conical X-ray source which improves the signal-to-noise ratio by allowing for an increased cone angle and, subsequently, a closer source-to-sample distance to be utilized compared to circular scanning setups (Wildenschild and Sheppard 2013). Furthermore, although extremely sensitive to sample misalignments, this allows for faster scan times, longer specimen scans, and allows for theoretically exact reconstruction of the sample that is free of artifacts (Varslot et al. 2011a, 2011b). A more in-depth explanation of both microCT equipment configurations and helical scanning reconstruction can be found in Wildenschild and Sheppard (2013) and (Varslot et al. 2011a, 2011b), respectively.

## SANIDINE

Feldspars are the most abundant constituents of common igneous rocks and, as such, are integral to many petrologic studies. Sanidine ([K,Na]AlSi $_3$ O $_8$ ; Or $_{37-100}$ ) is the dominant alkali feldspar found in volcanic rocks and frequently displays frequent chemical zoning. As it typically equilibrates at higher temperatures than other alkali feldspars, sanidine is prone to having greater amounts of elemental substitution (typically Ba $^{2+}$ , Sr $^{2+}$ , Ti $^{4+}$ , Fe $^{2+}$ , Fe $^{3+}$ , Mg $^{2+}$ ) in its crystal structure (Deer et al. 1966). Of these,

Ba<sup>2+</sup> substitution is the most common because of similar atomic radii between K<sup>+</sup> and Ba<sup>2+</sup> and is accommodated into sanidine in the following substitution (Icenhower and London 1996):

$$(Ba^{2+}, Sr^{2+}) + K^{+} + Al^{3+} = 2Na^{+} + Si^{4+}.$$
 (2)

Thus, Ba is a highly compatible element in sanidine and is often present at concentrations that range from hundreds of μg/g to weight percent levels. Barium zoning is also commonly observed in sanidine and other alkali feldspars from plutonic and volcanic rocks (e.g., Chambers et al. 2020; Rout et al. 2021). Specifically, sanidine populations that display frequent high (>1 wt%) Ba zones occur in many large ignimbrites (e.g., Bachmann et al. 2014; Szymanowski et al. 2017, 2019; Forni et al. 2018; Lubbers et al. 2020) from throughout the geologic record, implying that the processes responsible for forming them is also of importance in understanding the evolution of many silicic systems capable of producing large volcanic eruptions. Commonly proposed mechanisms for formation of these high-Ba zones are either localized cumulate melting (e.g., Bachmann et al. 2014; Wolff et al. 2015, 2020), mass transfer from a more mafic magma relatively enriched in Ba (e.g., Ginibre et al. 2004), or temperature cycling (Rout et al. 2021), however reconciling these mechanisms with other types of data (i.e., major element zoning, other trace element zoning, diffusive equilibration timescales, thermodynamic modeling) often introduces additional ambiguity, such that it is difficult to definitively discern between competing models (Shamloo and Till 2019). Interpretations are also complicated by the relatively slow rates of Ba diffusion in silicate melts (Singer et al. 1995; Zhang 2010), which can result in a decoupling of major and minor element behavior, and also by lack of accurate description of Ba partitioning as a function of pressure, temperature, and composition (P-T-X), reflecting the fact that alter-valent (i.e., 2+ to 1+) Ba partitioning into K sites in sanidine is also highly sensitive to changes in melt composition (Mcintire 1963). As a result, although Ba zoning has also been shown to be useful for understanding the timescales associated with recharge leading up to an eruption (Morgan and Blake 2006; Chamberlain et al. 2014; Till et al. 2015; Shamloo and Till 2019), the ultimate causes of this zonation remains incompletely understood. Furthermore, in addition to its petrologic importance, Ba also has a significantly higher mass attenuation coefficient than any other major stoichiometric component in sanidine (Table 1). We, therefore, hypothesize that changes in CT grayscale will largely correspond to changes in Ba concentration in sanidine, ultimately allowing us to better constrain 3D zoning of Ba in sanidine, potentially leading to a better understanding of the magmatic processes responsible for forming Ba zoning as well as their associated timescales, furthering our understanding of igneous systems in which sanidine is present.

#### **Methods**

#### Samples

To observe the relationship between CT data and sanidine composition, sanidines from several different volcanic rocks have been studied: the 35.3 Ma Kneeling Nun Tuff (Szymanowski et al. 2017) from the Mogollon-Datil Volcanic Field (MDVF); the 27.55 Ma Carpenter Ridge Tuff (Lipman and McIntosh 2008) from the Southern Rocky Mountain Volcanic Field (SRMVF); the 631 ka Lava Creek Tuff (Matthews et al. 2015) from Yellowstone caldera; and recent dome

**TABLE 1.** List of major stoichiometric cations found in sanidine, their atomic weight, and mass attenuation coefficient  $(\mu \cdot \rho^{-1})$  at 80 keV (i.e., the energy used in this experiment) showing that Ba has a significantly higher mass attenuation coefficient than all other cations

Element	Atomic weight (Amu)	80 keV mass attenuation coefficient (cm <sup>2</sup> ·g <sup>-1</sup> )
Na	22.990	0.1796
Al	26.982	0.2018
Si	28.085	0.2228
K	39.098	0.3251
Ca	40.078	0.3656
Fe	55.845	0.5952
Ba	137.330	3.9630

Note: Mass attenuation coefficients taken from Chantler (2000).

lavas from Taapaca volcano in northern Chile (e.g., Rout et al. 2021). These samples were chosen because they all show significant zoning in Ba contents and collectively also span a large range in both bulk rock compositions (i.e., dacite to rhyolite) and BaO (i.e., 0 to ~3.5 wt%) concentrations. Sanidine grains were mechanically separated and hand-picked using conventional crushing and picking methods. Once picked, selected sanidine grains were then mounted vertically in a thin epoxy rod ~3 mm in diameter and 40 mm tall such that they were completely encased by epoxy (Fig. 1). This geometry was selected to produce a shorter X-ray source to sample distance compared to 25 mm epoxy round mounts, while still allowing for many grains to be scanned at once using helical scanning. The shorter source-to-sample distance allows for higher spatial resolution data to be gathered as microCT data voxel size is proportional to sample distance from a conical X-ray source (Sheppard et al. 2014).

## MicroCT

MicroCT scans were acquired using Oregon State University's microCT facility (microct.oregonstate.edu). The OSU microCT X-ray source consists of a conebeam setup using a Hamamatsu L10711-19 specifically customized to microCT applications. The focal spot size is 630 nm, and X-rays are projected directly onto a 3000 × 3000 pixel Varex Paxscan amorphous silicon detector that incorporates a high-sensitivity CsI scintillator. Instrument settings utilized in this study are a voltage of 80 kV, current of 60 µA, and source to sample distance of 5 mm. While image resolution may be subject to debate, these settings resulted in a voxel size of 2.1–2.2 µm. Using helical scanning, the instrument captured a total of 5628 projections of the sample as it rotates through 360°. Maps of X-ray intensities for each sequential 2D frame were reconstructed using custom-built software that allows for helical retrieval and auto-focus alignment following the methodology of Varslot et al. (2011a). When fully reconstructed, a full scan produces a 3D volume that consists of a series of 2D digital grayscale images. A total of three scans were completed for this study over the span of 18 months, and throughout we found no issue with either beam hardening or ring artifacts in our data.

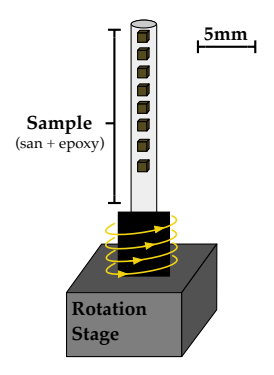


FIGURE 1. Schematic of the sample setup used in the microtomographic scanning. Sanidine grains were mounted vertically in a thin epoxy rod and placed in the sample holder on the helical rotation stage. This allowed for a source to sample distance of 5 mm, and the helical trajectory subsequently allowed for numerous grains to be scanned in one single (long) scan at high resolution. (Color online.)

**TABLE 2.** Standards utilized in EPMA experiment calibration for each element measured, along with the relative standard error and detection limit for each element measured

Standard	Element	Relative standard error (%)	Detection limit (μg/g)
ALBI	Na	0.40	334
SANI	Al	0.14	336
SANI	Si	0.12	684
SANI	K	0.17	438
NMNH 115900	Ca	21.61	357
NMNH 113498-	1 Fe	4.77	812
SANI	Ba	0.28	309

Notes: ALBI and SANI standards are synthetic albite and sanidine standards made by Astimex Scientific Ltd. and NMNH standards are from the collection at the Smithsonian Museum of Natural History. Established concentrations can be found in the Online Materials¹ Appendix 1.

## Electron probe microanalyzer

Backscatter electron (BSE) images and major element analyses of sanidine grains were obtained using a Cameca SX100 electron probe microanalyzer (EPMA) at Oregon State University. For all analyses, a focused beam of 5 µm, 15 kV accelerating voltage, and 30 nA current was used. Reference materials used as standards and detection limits for each element can be found in Table 2. Two approaches were taken to facilitate a direct comparison of data and 2D images from the EPMA to 3D microCT images. Initially, individual crystals were sectioned, polished, and imaged using BSE after microCT images were taken, and we then selected the section in the microCT volume that most closely matched the 2D section. This proved challenging in some cases, however, and for subsequent analyses, crystals were sectioned and analyzed via EPMA prior to microCT to locate crystals with the largest amount of variation of Ba contents for analysis. After CT scans, corresponding BSE and CT 2D sections were chosen for comparison. To maintain as close as a 1:1 comparison between EPMA and CT data, CT grayscale profiles mimicked the size of the EPMA beam as close as possible (i.e., profile values are the average of 3 pixels along the same path as the EPMA transect and spot values are the average of a 3 × 3 pixel area). This produces CT transects that have a width of 6.2  $\mu$ m and spots that have an area of 37.21  $\mu$ m<sup>2</sup> compared to 5  $\mu$ m and 25  $\mu$ m<sup>2</sup> on the EPMA, respectively. Uncertainties in CT grayscale value were determined by taking the standard deviation of a 3 × 3 pixel area (e.g., approximately the size of one EPMA spot) and range from 40 to 300. In all plots and calculations, we assume maximum observed uncertainty and report the mean grayscale value  $\pm 300$ , which is 1-2% of the overall attenuation signal.

## Image processing

In microCT data, variations in the linear attenuation coefficient of a material are observed as changes in grayscale intensity in the reconstructed 3D volumes (Denison et al. 1997). Linear attenuation coefficients of sanidine areas analyzed by EPMA in this study were also predicted using Mccullough (1975):

$$\mu_{l} = \mu_{m(total)} \rho_{mineral} \tag{3}$$

where  $\mu_m$  is the mass attenuation coefficient taken from Chantler (2000) and  $\rho$  is the density of the mineral. Mass attenuation coefficients of mixtures (i.e., sanidine) were also calculated using (McCullough 1975):

$$\mu_{m(total)} = \sum_{i=1}^{n} \omega_{i} \left(\mu_{m}\right)_{i} \tag{4}$$

where  $\mu_m$  is the mass attenuation coefficient and  $\omega$  is the proportion by weight of stoichiometric component *i*. Chemical zoning in minerals, if sufficiently different, will be observed as changes in X-ray attenuation (Eqs. 3–4).

The software/coding packages used for image processing in this project are shown in Table 3. Data sets generated from the initial 3D volume were cropped into smaller, more manageable sizes that: (1) reflect individual minerals; and (2) reduce file size substantially to make subsequent processing achievable on a

standard personal laptop. One of the goals of this project was also to make the methodology as open source and accessible as possible. Because of this, all the image processing besides the cropping and slicing of data sets (Avizo) was done in either Fiji/ImageJ or via scripting in Python. While we note both Python and Fiji/ImageJ are capable of cropping and resampling data sets on personal computers, the large file size of an individual scan (i.e., >100GB) necessitated the use of the OSU microCT lab processing workstation. Built on top of the Python package scikit-image [https://scikit-image.org/ (Van Der Walt et al. 2014)], we have also created a Python module, CTPy [https://github.com/jlubbersgeo/ctpy (Lubbers 2020)], to help make the image segmentation process more streamlined.

To quantify the number of distinct phases or regions within a sample, a histogram was generated where each peak generally corresponds to a specific phase/region. For materials with different attenuation (e.g., sanidine, epoxy, air), the histogram peaks of CT grayscale were typically distinct (e.g., Fig. 2). When dealing with intracrystalline zoning in minerals, however, we found that although there are observable differences in grayscale within minerals (Fig. 2a: right) the histogram created from these two zones still overlapped significantly (Fig. 2a: left). To refine these histograms by removing inherent noise from the data while still preserving crucial textural information, we applied a non-local means (NLM) algorithm (Buades et al. 2005; Van Der Walt et al. 2014) to each individual 2D image. This was implemented using scikit-image and was completed using a block size of 10 pixels and a search window of 10 pixels. After this filter was applied, we typically observed four peaks in the slice data (background, epoxy, mineral zone 1, mineral zone 2; Fig. 2b left) that match what we qualitatively see in grayscale (Fig. 2b right). This approach allowed us to better quantify areas and volumes of individual mineral zones via image segmentation (i.e., partitioning the image into distinct regions/segments based on a set of characteristics).

Image segmentation was completed using the watershed algorithm (Vincent and Soille 1991; Roerdink and Meijster 2000; Van Der Walt et al. 2014). Using predefined markers, the watershed algorithm identifies the spatial extent of the two regions of interest. For our sanidine grains, we create these markers by applying the Sobel gradient operator to create an image mask where pixel values correspond to their intensity gradient (Jähne et al. 1999; Van Der Walt et al. 2014). With sanidines

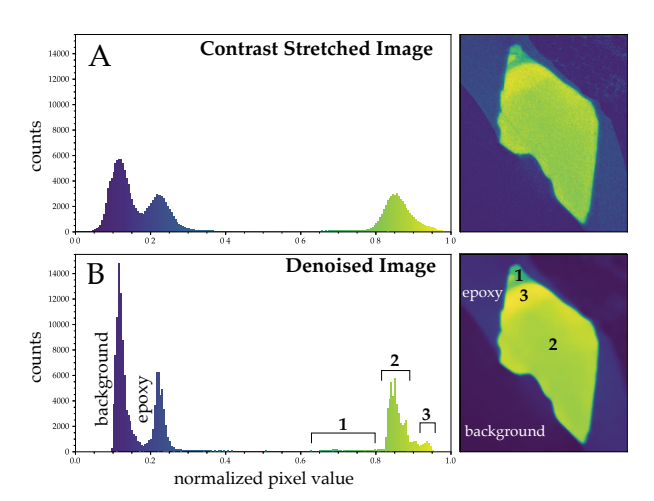


FIGURE 2. Individual CT slices extracted from the 3D data set and their corresponding histograms. (a) Raw, unfiltered data that shows changes in pixel value within the mineral, however there is significant overlap between the mineral peaks (3 and 4). (b) Same slice processed using a non-local means filter (using Python's scikit-image). The slice histogram now has resolvable peaks that better correspond to distinct mineral regions and allows for reliable image segmentation, and subsequent quantification. (Color online.)

TABLE 3. List of programs/software used in this research and what each was used for

Program/software

Avizo

Data set cropping, 2D slicing of data set (both random and non-random).

Fiji/ImageJ (Schneider et al. 2012)

Python/JupyterLab

Data set cropping, image denoising, image segmentation, image statistics, interactive volume reconstructions.

Utilizes the package scikit-image (Van Der Walt et al. 2014) and volume reconstructions require package K3D-jupyter.

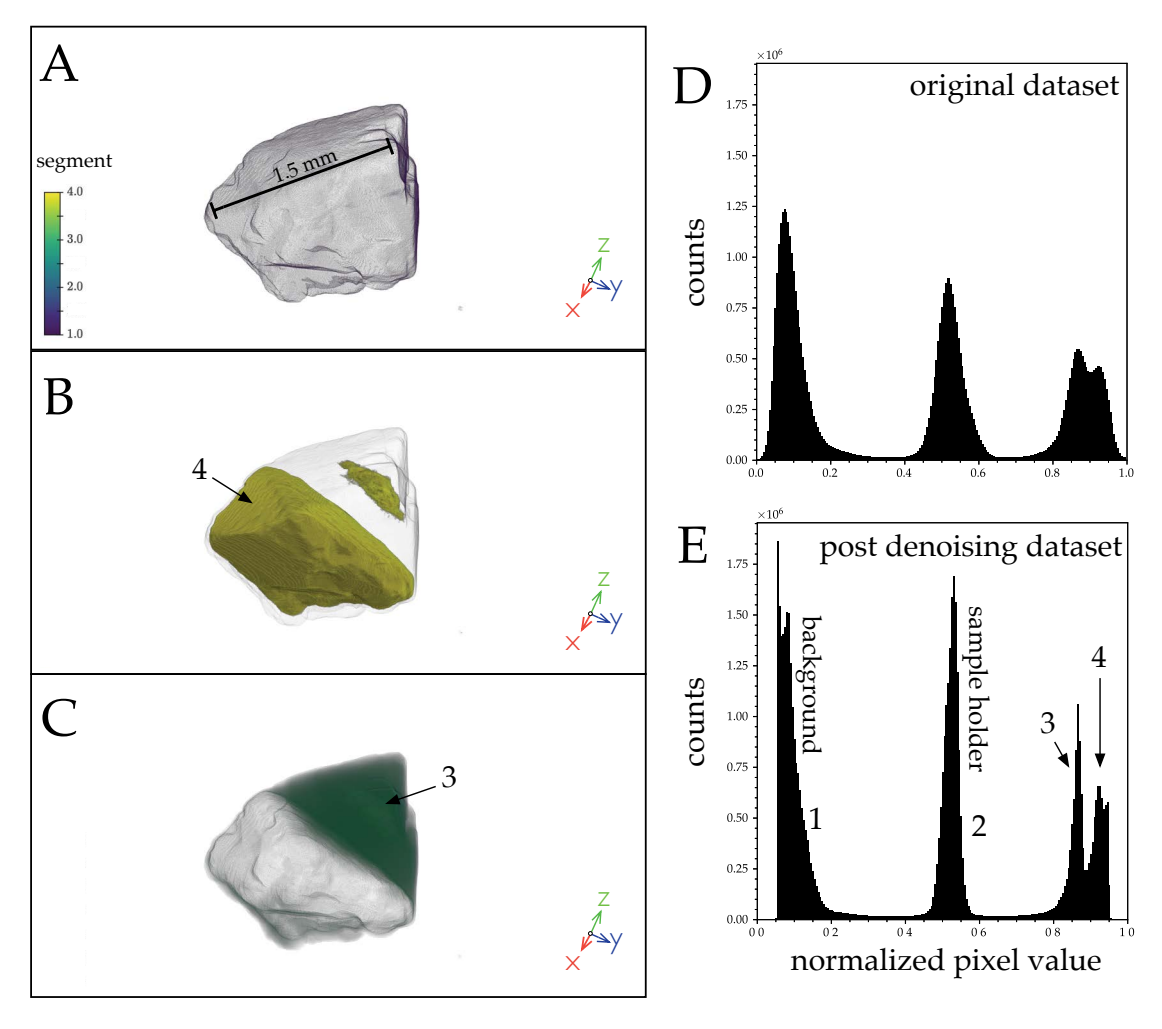


FIGURE 3. 3D rendering of a segmented sanidine from the Kneeling Nun Tuff and the same grain shown in Figure 2. (a, b, and c) All have the same orientation. (a) Whole mineral. (b) Mineral zone that corresponds to peak 4 in the post denoising histogram. (c) Mineral zone that corresponds to peak 3 in the post denoising histogram. (d) Raw CT data histogram and (e) denoised histogram justifying the segments used to train the watershed algorithm. (Color online.)

segmented into distinct regions based on both grayscale value and location, three-dimensional reconstructions of these volumes were made (Figs. 3a–3c).

#### RESULTS

Histograms for each sanidine crystal can be found in Online Materials¹ Figure OM1 and compositional data for each crystal gathered using EPMA can be found in Online Materials¹ Appendix 1. Most samples display multiple CT grayscale feldspar peaks after passing through the non-local means denoising filter (e.g., Fig. 3e), except for Lava Creek Tuff (LCT-B) sanidines which typically only display one. Likewise, backscattered electron (BSE) imaging of LCT-B sanidines also shows little to no grayscale zoning, whereas sanidines from the other samples display frequent grayscale zoning (Fig. 4). BaO concentrations in sanidines measured range from near detection limit (~300 ppm) to 3.7 wt% and brighter BSE zones correspond to higher BaO contents in all 2D sections analyzed. In the following section, the relationship between CT grayscale and sanidine composition is further explored.

## DISCUSSION

## Geochemical controls on X-ray attenuation in sanidine

A first-order observation in the denoised histograms of sanidine microCT data is that there are multiple peaks corresponding to regions within the minerals that attenuate X-rays to different degrees (Fig. 3e). To translate this observation to useful 3D compositional information, we first need to investigate the controls on X-ray attenuation in sanidine. Equation 3 shows that the mass attenuation coefficient ( $\mu_m$ ), and subsequently linear attenuation coefficient ( $\mu_1$ ), of a mixture can be predicted based on the stoichiometric proportions of all elements within a mixture and individual mass attenuation coefficients for a given energy. Because major element chemistry totals measured via EPMA sum to close to 100 wt% (Online Materials<sup>1</sup> Appendix 1), they are sufficient to estimate mass attenuation coefficients. Trace elements present in lower concentrations (e.g., Sr, Mg, REE, Pb, etc.) can also be included in this calculation, although typically the lower concentrations mean that attenuation characteristics

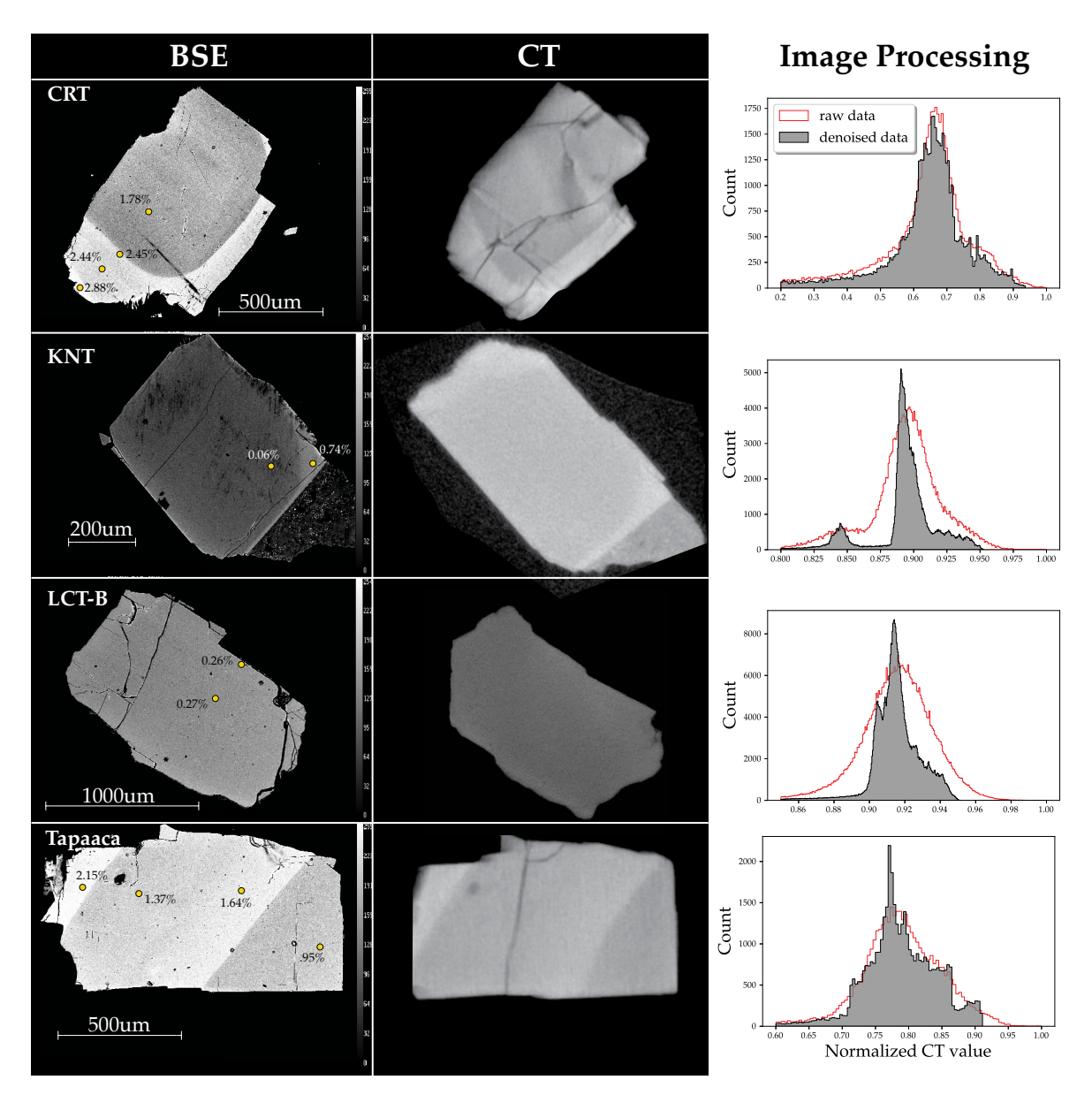


FIGURE 4. Representative sanidine grains from each system studied comparing BSE (left) and CT (middle) grayscale images for similar 2D slices through the same grain. Yellow spots annotated on BSE images indicate locations for EPMA spot analyses and BaO concentrations are listed next to each spot. The right panel shows histograms of normalized CT grayscale values for both raw data (red line) and denoised data (black line with gray fill) for each grain and illustrates its ability to sufficiently remove Gaussian noise such that mineral zoning in CT can be quantified via image segmentation methods. (Color online.)

will have a lesser impact on overall attenuation.

In Figures 5 and 6, we compare the composition of the sanidine with its calculated linear attenuation coefficients and the observed CT grayscale values, respectively. Calculated linear attenuation values and CT grayscale values correlate strongly with observed sanidine composition (Figs. 5 and 6). This is consistent with grayscale intensity being directly related to the linear attenuation coefficient for a given voxel (Denison et al. 1997). Moreover, although calculated linear attenuation coefficients show weak correlations with SiO<sub>2</sub>, CaO, and Na<sub>2</sub>O in some samples, for all samples Ba contents are very strongly

correlated (Fig. 5), suggesting that Ba is the primary control on X-ray attenuation and that changes in Ba contents are reflected in the observed changes in grayscale. Other elements display no clear relationship between changes in concentration and changes in calculated linear attenuation coefficient or voxel grayscale in sanidine (Fig. 5). Although Ba is present at lower concentrations than other stoichiometrically important components, the relatively high atomic weight and resulting photoelectric X-ray attenuation above the K-shell edge of Ba (particularly relative to the other elements present) coupled with the large variations evident in Ba strongly suggest that Ba is the primary control

on X-ray attenuation in sanidine under the scanning conditions used in this study.

To further test this hypothesis, we have also compared measured CT grayscale and measured Ba contents along transects across regions where Ba contents change substantially (Fig. 7). In these examples, we again observe that CT grayscale is strongly correlated with Ba contents, and not with other elements. Figure 8 quantifies both the global and local relationships observed between BaO in the different sanidines studied for this experiment. The data suggest that overall increases in BaO will result in an increase in CT grayscale (Fig. 8a) and follows the relationship:

BaO (wt%) =  $(3.4 \times 10^{-4} \pm 1.28 \times 10^{-5})X - (5.974 \pm 0.25)$  (5) where *X* is the CT grayscale value. The RMSE for this relationship is 0.275. Rewritten in terms of ppm Ba, the relationship is:

Ba (ppm) = 
$$(0.1055 \pm 0.004)X - (1867.067 \pm 78.023)$$
 (6)

with a RMSE of 86. Although a single relationship can be used to define the impact of Ba contents of X-ray attenuation, the relatively high RMSE and the observation that sanidine from different samples fall into distinct regions on the plot of BaO vs. CT grayscale (and define different trends) in Figure 8b suggest that there may be additional minor controls on X-ray attenuation. As all CT scans were done with the same setup conditions,

we hypothesize that the small variations in the exact relation between BaO and X-ray attenuation are due to other elements also contributing more minor changes to the linear attenuation coefficient, although it is also possible that this variation may be due in some part to slight changes in detector sensitivity across different scans. For example, we see in both the LCTB and CRT that CaO and Na<sub>2</sub>O also have linear relationships with CT grayscale value (Fig. 6); however, the slope of this relationship is much greater in the CRT than it is in the LCTB.

To further quantify the influence other elements have on the overall CT attenuation, we utilized several supervised machine learning regression algorithms, specifically, the random forest (Breiman 2001) and extremely randomized trees (ERT; Geurts et al. 2006) algorithms as they performed the best out of all algorithms tested (e.g., highest R<sup>2</sup> and lowest RMSE values). These algorithms were employed via the scikit-learn package [https://scikit-learn.org/ (Pedregosa et al. 2011)] in Python as it is: (1) open-source and (2) allows one to easily implement both supervised and unsupervised machine learning algorithms (e.g., Petrelli et al. 2020). In brief, our data was split randomly into both training and test data sets, where they consisted of random subsamples from each system studied in this experiment to be representative of a wide range of both geochemical characteristics and geologic settings. Once split into training and test data sets, each was standardized and further separated into

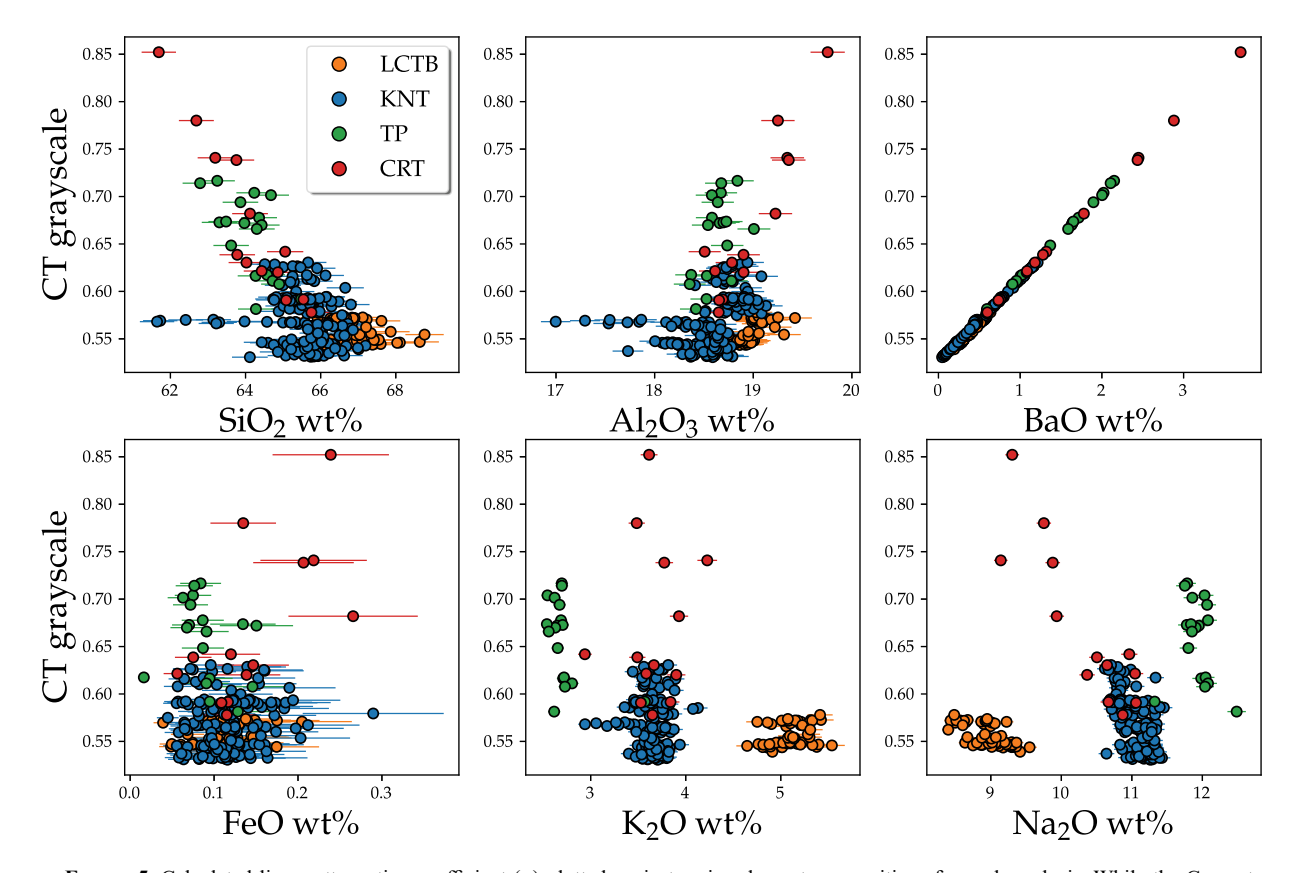


**FIGURE 5.** Calculated linear attenuation coefficient ( $\mu$ ) plotted against major element compositions for each analysis. While the Carpenter Ridge Tuff displays weak linear correlations between  $\mu$  and CaO and Na<sub>2</sub>O, BaO shows strong linear correlations with  $\mu$  for all sanidines studied in this project. (Color online.)

features (i.e., wt% oxide measurements) and a target (i.e., CT grayscale value). While multiple linear regression also offers a way to incorporate the influence of multiple features on a given target, we prefer the ERT and random forest algorithms as they have both better performance metrics (Fig. 9) and allow us to quantify the relative importance each feature has on predicting a target value without having to deal with issues related to multicollinearity (e.g., SiO<sub>2</sub>, Al<sub>2</sub>O<sub>3</sub>) that cause multiple regression coefficients to have limited predictive power. We find that both ERT and random forest algorithms predict observed CT values well (Fig. 10a) as well as further reinforce the importance of Ba in controlling attenuation Figure 10b.

## Observing chemical zoning in 3D

Having established the geochemical controls on X-ray attenuation in sanidine now allows us to both observe and quantify chemical zoning in 3D. Using image segmentation previously outlined in the "Image Processing" section, we segment individual sanidine grains into "high" (e.g., Fig. 3e peak 4) and "low" (e.g., Fig. 3e peak 3) Ba zones for KNT and LCT-B sanidines (Fig. 11). While the number of segmented regions is ultimately user defined and specific to individual data sets, the designation of distinct high-and low-Ba zones are justified based on: (1) CT data histograms (e.g., Fig. 3e); and (2) previous literature illustrating high- and low-Ba zones found in sanidines from many of the systems studied

(Bachmann et al. 2014; Shamloo and Till 2019; Szymanowski et al. 2019; Rout et al. 2021).

Defining two zones based on Ba also allows us to study the 3D geometry of these regions, and although our sample set is still somewhat limited, we observe a range of different zoning types. Some high-Ba zones were observed as concentric rims (Figs. 11a and 11c), consistent with a simple view of progressive crystal growth from magmas with different Ba contents, but other zones also display more complex geometric relationships, such as in intermediate zones between the crystal core and rim, (Figs. 11b, 11d, and 11e). The observation of intermediate high-Ba zones is important, as it implies that the magma reservoir processes responsible for producing these zones are not tied to eruption or initiation of eruption but rather that they occur within a magma reservoir during ongoing magma storage and evolution. This aligns with recent thermal models, showing that large silicic magma reservoirs can reside in the upper crust long periods of time (Gelman et al. 2013) and accommodate volume/pressure changes related to rejuvenation to promote growth rather than eruption (de Silva and Gregg 2014).

We also find that some KNT sanidine crystals have high-Ba zones that were largely discontinuous (i.e., they did not form a zone around/throughout the entire grain), did not have a uniform thickness, and were never cores of grains. While we note that the markers used for the watershed algorithm may influence the final geometry of mineral zone reconstructions, these observations hold

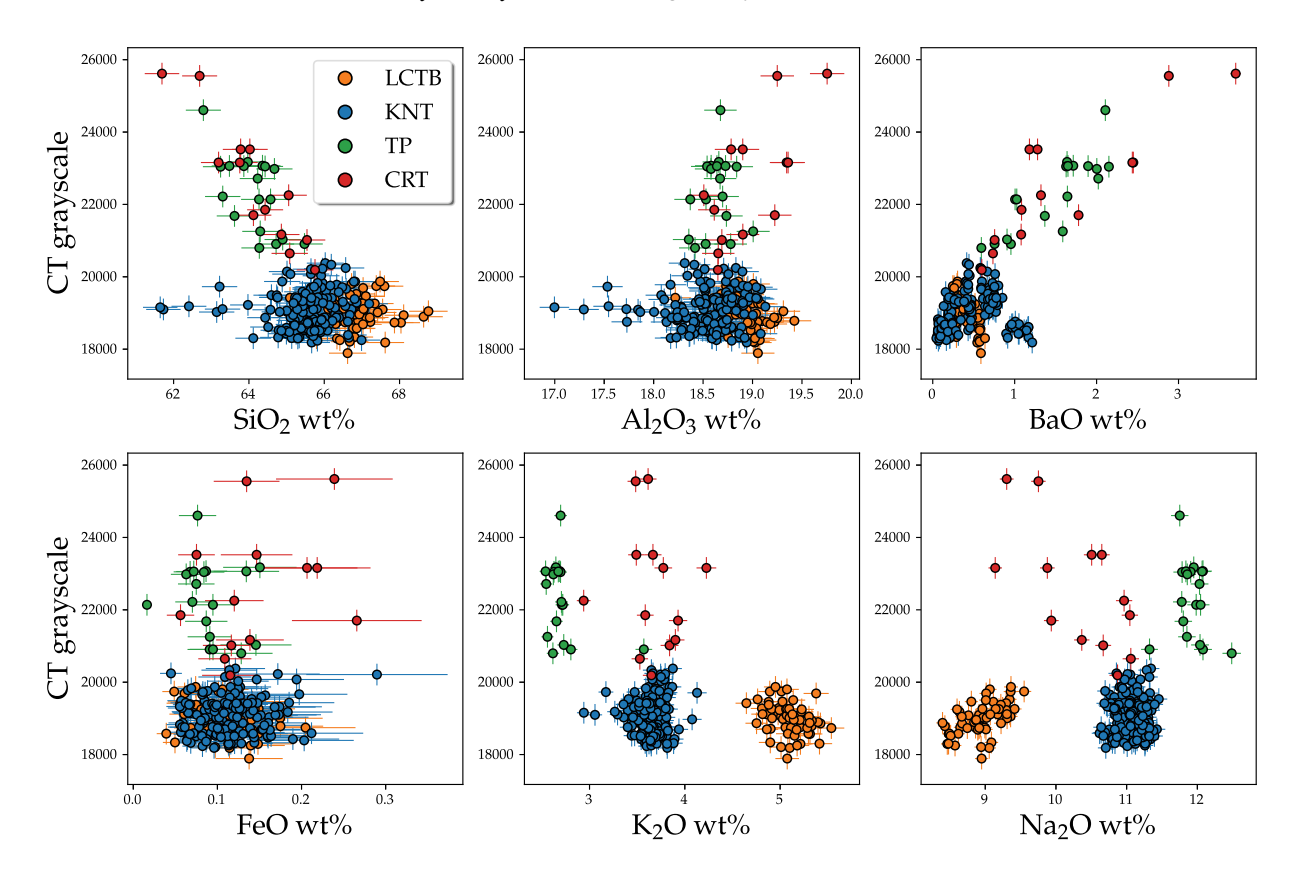


FIGURE 6. Observed CT grayscale for the same location on a given sanidine that EPMA analyses were completed, plotted against major element compositions for the same location. The shape of the observed CT grayscale vs. major element relationships qualitatively looks like that described by the  $\mu$  vs. major element relationships shown in Figure 5. This agrees with Denison et al. (1997), which shows that CT grayscale is linearly related to  $\mu$ . (Color online.)

► FIGURE Comparison of BSE image and CT grayscale image for the same plane through a KNT sanidine that was scanned via microCT prior to EPMA analysis. Yellow lines illustrate location of the EPMA and CT transects that are plotted below. Both show the same relative changes in magnitude and have similar slopes. This further adds to the relationships shown in Figure 4 by adding in a spatial component and shows that CT grayscale is largely controlled by Ba concentrations throughout the mineral. (Color online.)

3.0

2.0

1.0

0.5

19000

BaO wt% 2.5

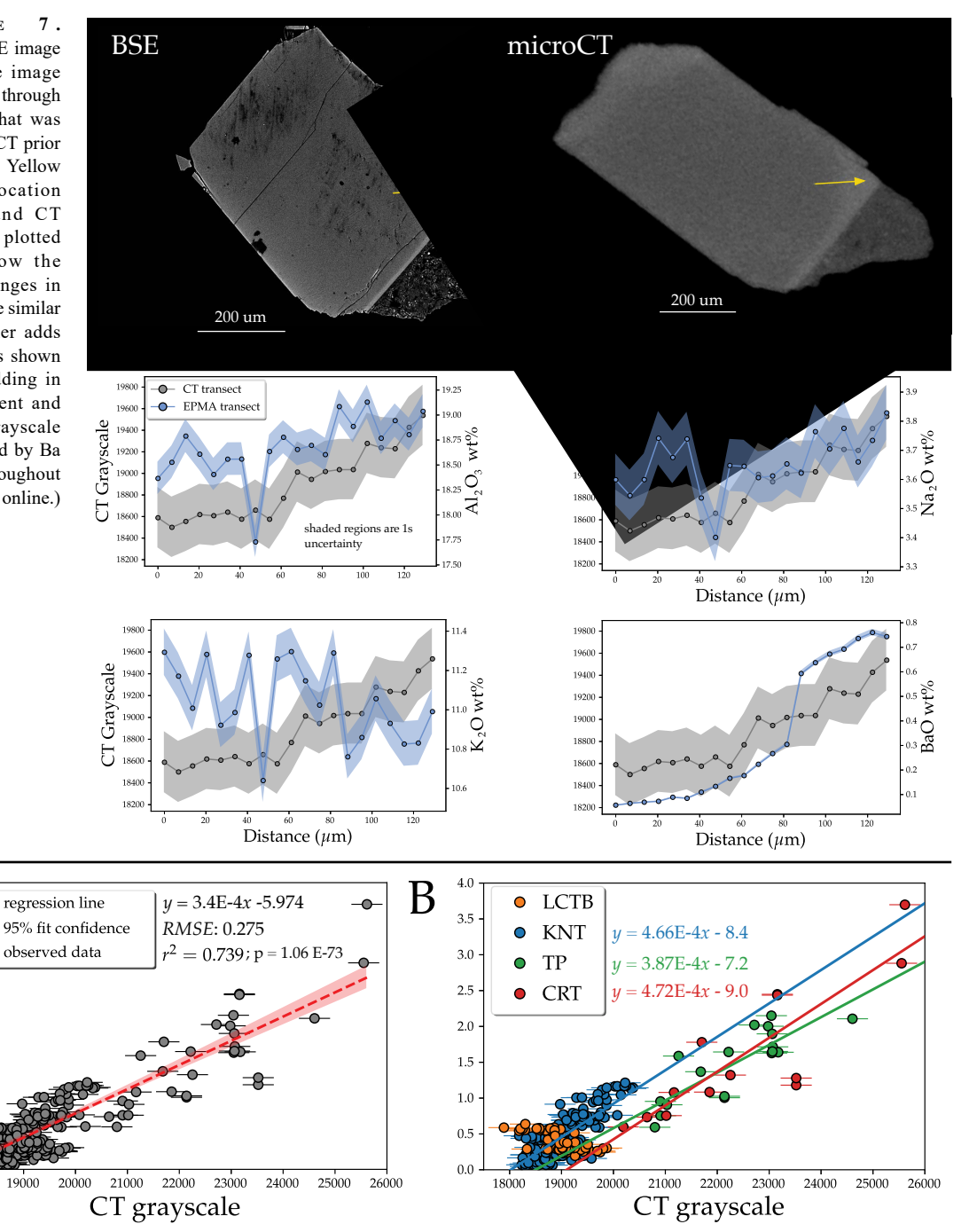
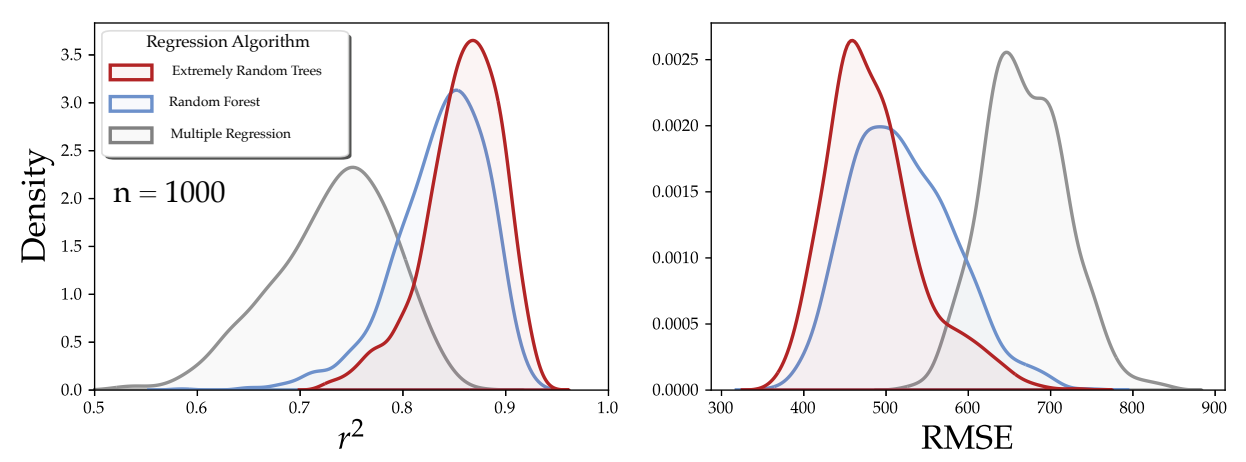


FIGURE 8. (a) Regression for Ba vs. CT relationship for all sanidines studied in this experiment. (b) Regression for Ba vs. CT for each individual eruption studied in this experiment. Note there is no regression for the LCTB, as it displayed too narrow a range in BaO concentrations. While KNT, TP, and CRT sanidines all show a linear correlation between BaO and CT grayscale, the parameters that define each relationship vary slightly, however suggest that although BaO is largely responsible for controlling X-ray attenuation in sanidine, its influence on each system is not the same. (Color online.)

true for all grains scanned from the KNT, suggesting that they are representative of features of the sanidines from this system. Previously, these high-Ba zones have been interpreted as the result of cumulate remelting in a thermally heterogeneous magma reservoir prior to eruption (Szymanowski et al. 2019). Our 3D reconstructions

of high-Ba zones agree with this interpretation, as we argue that progressive mineral growth in a closed system is unlikely to produce the wide array of geometries observed here. Rather, as mineral zoning reflects the thermochemical conditions in which the mineral grew, the heterogeneous mineral zoning geometries observed are



**FIGURE 9.**  $R^2$  and root mean squared error (RMSE) of predicted CT grayscale results of a Monte Carlo simulation in which each machine learning algorithm for predicting CT values was run 1000 times. For every iteration, the splitting, training, and validation steps for each algorithm were randomized to remove bias of any one iteration on the overall interpretation of a given algorithm's accuracy and precision. The extremely random trees (ERT) regression algorithm performs the best by both  $R^2$  ( $\mu = 0.86$ ) and RMSE ( $\mu = 487$ ) metrics, therefore making it the preferred algorithm for predicting CT grayscale in this study. (Color online.)

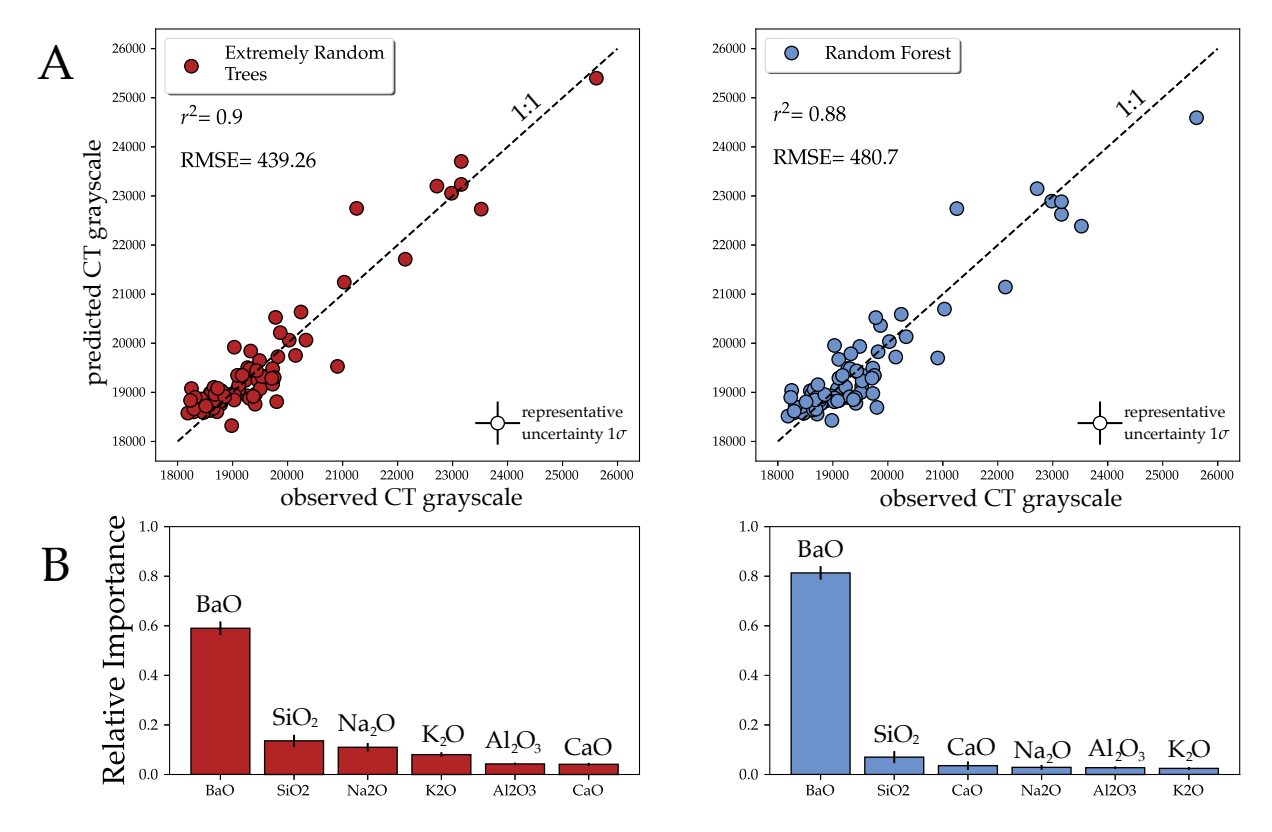
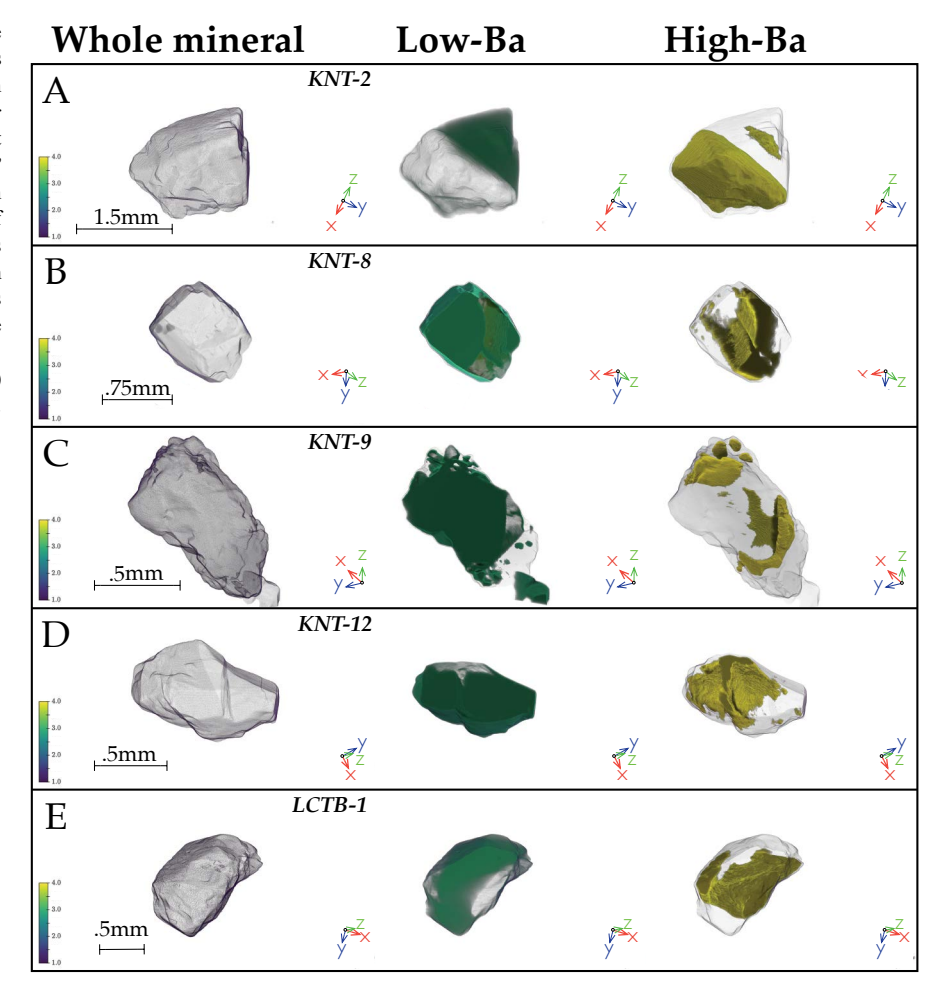


FIGURE 10. (a) Scatter plot of predicted vs. observed CT grayscale values from the ERT (left) and random forest (right) algorithms for one of the random iterations of the Monte Carlo simulation shown in Figure 9 illustrating that they: (1) accurately predict the observed CT values (e.g., falls along a 1:1 predicted vs. observed line); and (2) produce low-RMSE values relative to the overall attenuation signal (i.e., <3%). (b) Bar charts displaying the relative importance of each feature used in the regression algorithms. The height of the bars is the mean value of each feature's importance from the Monte Carlo simulation and error bars are 1σ uncertainties for each mean value. Note, the total height of all the bars is equal to 1. Single feature values closer to 0 are not as useful at predicting the target and values closer to 1 are extremely useful at predicting the target. Barium displays the highest feature importance in both algorithms and accounts for most of the information required to accurately predict CT grayscale values, suggesting it is largely responsible for controlling X-ray attenuation in sanidine. (Color online.)

FIGURE 11. 3D volume reconstructions of chosen sanidines segmented in this study. Left column is entire mineral outline, center column green isosurfaces represent extent of zones classified as "low-Ba" within the grain, and right column yellow isosurfaces outline extent of areas within the grain classified as "high-Ba." Rows A-D are grains from the Kneeling Nun Tuff and row E is a Lava Creek Tuff-B sanidine. Note that zoning patterns are frequently: (1) not always concentric and (2) not always on the rims of the grain. (Color online.)



most likely the result of reservoir scale heterogeneities. Further CT-based works offer the potential for quantitatively examining the shape and distribution of high-Ba zones in these samples and in other igneous rocks to test models for magma genesis and evolution.

# IMPLICATIONS FOR MINERAL ZONING STUDIES Gradient variability between two zones

Assessing the shape of the concentration gradient between two chemical zones is critical for understanding magma evolution and also for petrologic approaches such as diffusion chronometry. Commonly this approach utilizes either thin sections or mineral grain mounts to analyze the 1D changes in chemistry across a concentration gradient (i.e., chemical zone boundary) within a mineral. Production of thin sections or grain mounts commonly produces random or near-random sectioning of crystals, and this can strongly influence the nature of a given concentration gradient (Shea et al. 2015). Slices that are near perpendicular to compositional zoning will have a steeper gradient between zones than slices that are more oblique. At their extremes, slicing perpendicular to zoning will reflect the true gradient shape, while slicing parallel to zoning will show no zoning at all. This effect has been studied numerically using synthetic crystals (Shea

et al. 2015; Krimer and Costa 2017), however, our information on the 3D distribution of Ba in sanidine allows us to also study this in natural crystals, and simulate the 2D sectioning process by randomly slicing a 3D CT volume. We can then compare this with the profile extracted from a slice perpendicular to the gradient to see how the shape of that gradient changes with the slicing orientation.

As expected, significant variability can be introduced into the shape of gradients between zones simply by randomly slicing the same grain through its center (Fig. 12). When combined with slicing orientation information, we see that as slices become more perpendicular to the 2D plane that represents the true gradient, profiles both increase in slope and decrease in width (Fig. 13). Looking at the distribution of slopes across a range of random slice numbers it becomes clear that the highest number of random slices are not centered around the true slope, but rather much shallower (Fig. 14c) implying that the majority of 2D section profiles from random slices do not reflect the true shape of the concentration gradient between zones.

Similarly, we find that the width of a given concentration gradient is not accurately represented by the mean of random slices and overestimates the true width (Fig. 14a). Random slicing of

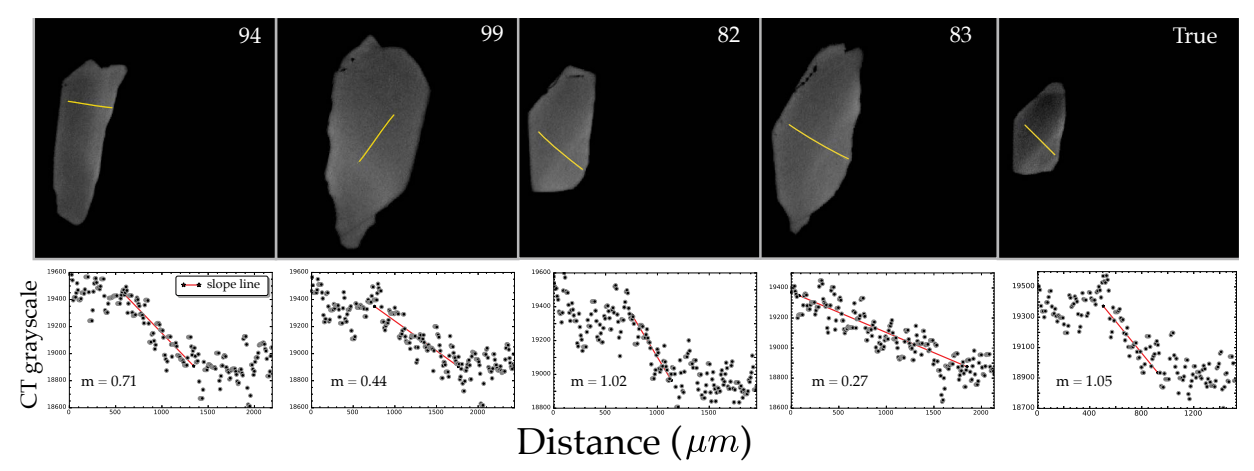


FIGURE 12. Random 2D slices through the CT stack for grain LCTB-1 shown in Figure 11e and their corresponding 1D CT grayscale profiles. CT grayscale profiles were chosen by making a transect perpendicular to observed grayscale zoning in each random slice. The slope for each profile is indicated by the red line and is calculated chosen based where there is an abrupt change in grayscale values and the grayscale values on each side of the gradient. Grayscale profiles display a wide range of widths and slopes, illustrating the effect that random slicing through a grain has on the interpretation of chemical zoning. (Color online.)

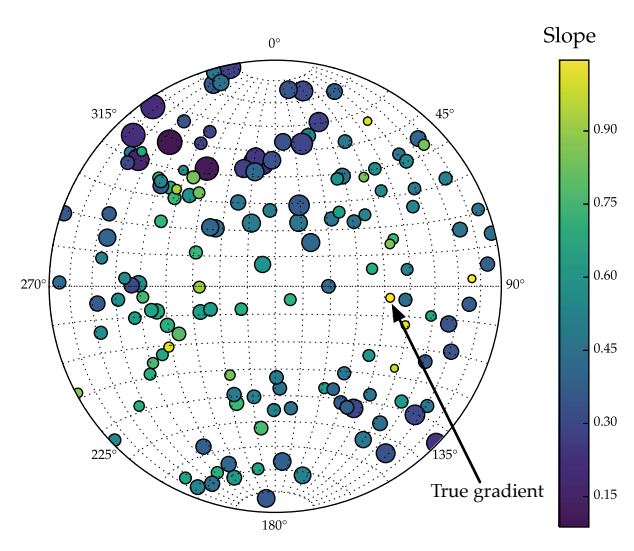


FIGURE 13. Stereonet of 150 random slices through crystal LCTB-1 shown in Figure 11e, where each pole to the plane for a given random slice is a spot on the stereonet. Here, degrees are in arbitrary 3D space, not cardinal directions. Colors of each spot are mapped to the slope of the concentration gradient, while the size of each spot is mapped to the width. Overall, shallower slopes and longer profile widths are associated with slices that are more parallel to the true gradient orientation (e.g., upper left on the stereonet). (Color online.)

grain across a concentration gradient, however, does accurately capture the height of a concentration gradient (Fig. 14b). To accurately obtain concentration gradient information (e.g., slope, width, height), Shea and others (2015) suggest that by following a list of criteria (e.g., discarding small grains, constructing profiles away from crystal corners, avoiding profiles with dipping plateaus, when concentric zoning is present avoid zoning that is asymmetric), constructing profiles from 2D sections can more accurately portray the true gradient shape if ~20 well-chosen analytical profiles are constructed. However, it is also true that

when 3D information is available, it is possible to no longer speculate about the shape of the concentration gradient between zones but rather to directly observe it by going into the CT stack and extracting a slice perpendicular to CT grayscale zoning. If CT grayscale is governed by changes in a specific element (e.g., Ba in sanidine, Fe-Mg differences in olivine), then accurate 1D, 2D, and 3D diffusion modeling can be completed without ambiguity as to whether or not we are measuring the true shape of the concentration gradient.

## Beyond barium in sanidine

While it has been shown here that 3D chemical zoning in Ba can be observed in sanidine, in theory, this methodology should not be limited to just sanidine if chemical zones within minerals have a sufficient difference in linear attenuation coefficient. The absolute difference required to observe chemical zoning using microCT, however, depends on the voxel resolution used for imaging and the machine settings (i.e., voltage, current, exposure time) used, which affect image contrast (signal-to-noise ratio). Because the photoelectric effect (and its sensitivity to atomic number) and density are the dominant attenuation mechanisms for energies used in scanning geologic samples, large changes in heavy elements should be relatively easy to observe. This makes minerals with proportionally high concentrations and zoning of heavier elements, such as rare earth elements, actinides (U, Th), and heavier transition metals (e.g., Pb), likely candidates for observing chemical zoning using microCT if they are present in sufficient quantity. Different Fe-Mg olivine populations have already been successfully identified using both monochromatic (Pankhurst et al. 2018) and polychromatic microCT (Pankhurst et al. 2014), making the intracrystalline investigation of Fe-Mg zoning another worthwhile pursuit (cf. NIST Standard Reference Database 66, Chantler 2000).

One of the current limitations of industrial microCT devices is that they emit polychromatic radiation and are subject to potential imaging artifacts (e.g., beam hardening) and limitations in X-ray output, requiring longer scan times. To overcome these,

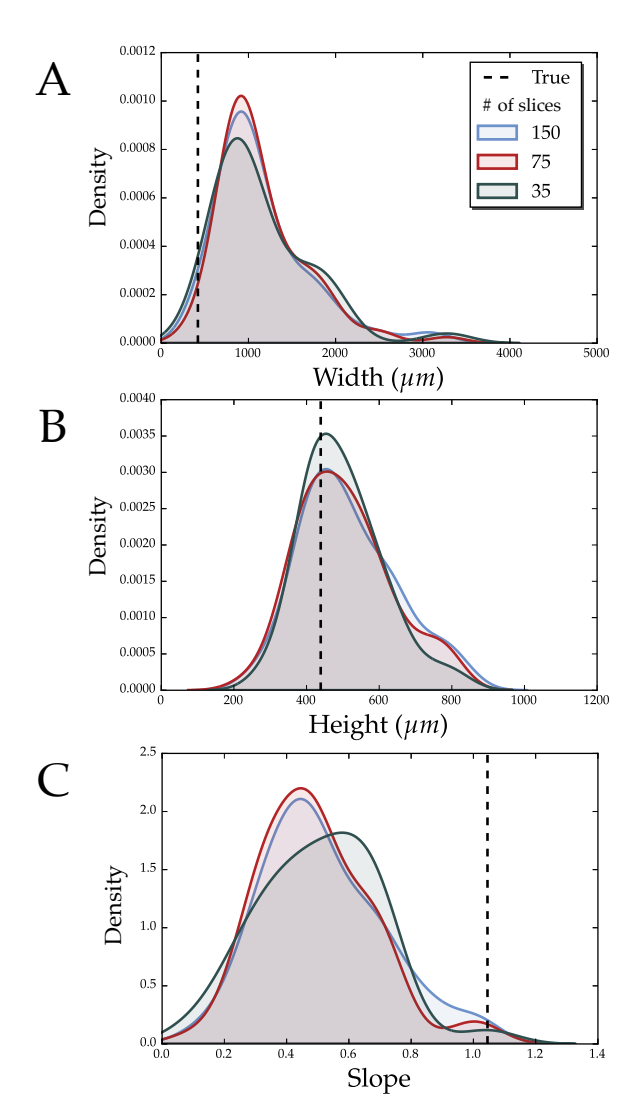


FIGURE 14. Breakdown of random slicing exercise in which 35, 75, and 150 random slices were generated through the center of grain LCTB-1, shown in Figure 10e. Slices were through the center of the grain to ensure that the concentration gradient was intersected by the slice. (a) Kernel density estimates (KDE) of concentration gradient widths illustrating how the true width of a concentration gradient is overestimated by majority of slices (b) KDE plot for gradient heights. Here, the random slicing exercise suggests that the mean of random slicing more accurately portrays the height of a given concentration gradient (c) KDE plot for gradient slopes. As in a, the majority of slices do not reflect the true slope of a given concentration gradient and the majority of slopes generated from random slicing are significantly less than the true slope of the concentration gradient. (Color online.)

synchrotron sources are typically used (e.g., Hanna and Ketcham 2017). The large amount of flux produced by a synchrotron source allows for beam filtration and fine-scale "tuning" over a given energy range (Willmott 2011). The use of this in the petrology community is minimal (e.g., Gualda and Rivers 2006; Gualda et al. 2010; Pamukcu and Gualda 2010; Pankhurst et al. 2018), however, the potential is very high, as it allows for one to theoretically focus in on a given element, and scanning above and below the photoelectric absorption edge for that

element to allow for subtraction tomography. If utilized, the benefit of this would be twofold: (1) better elemental resolving power and (2) a range of lower beam energies to subject the sample to, further increasing the contrast in grayscale between chemical zones. This increased contrast would then lead to more accurate segmentation of geochemically distinct phases and allow us to better view the complexities of mineral zoning in 3D and the interpretations that come from its investigation (e.g., diffusion chronometry, mineral growth/dissolution, glomerocryst formation).

### ACKNOWLEDGMENTS AND FUNDING

We thank the many people who provided samples for this study: Dawid Szymanowski and Ben Ellis (Kneeling Nun Tuff); Olivier Bachmann and Chad Deering (Carpenter Ridge Tuff); Hannah Shamloo and Christy Till (Lava Creek Tuff). We also thank Frank Tepley and Marie Takach for their expertise and advice gathering microprobe data. This research was supported by National Science Foundation grant NSF-EAR 1654275.

### REFERENCES CITED

Anderson, A.T. (1976) Magma mixing: petrological process and volcanological tool. Journal of Volcanology and Geothermal Research, 1, 3–33.

Arzilli, F., Mancini, L., Voltolini, M., Cicconi, M.R., Mohammadi, S., Giuli, G., Mainprice, D., Paris, E., Barou, F., and Carroll, M.R. (2015) Near-liquidus growth of feldspar spherulites in trachytic melts: 3D morphologies and implications in crystallization mechanisms. Lithos, 216-217, 93–105.

Arzilli, F., Polacci, M., Landi, P., Giordano, D., Baker, D.R., and Mancini, L. (2016) A novel protocol for resolving feldspar crystals in synchrotron X-ray microtomographic images of crystallized natural magmas and synthetic analogs. American Mineralogist, 101, 2301–2311.

Bachmann, O., Deering, C.D., Lipman, P.W., and Plummer, C. (2014) Building zoned ignimbrites by recycling silicic cumulates: insight from the 1,000 km<sup>3</sup> Carpenter Ridge Tuff, CO. Contributions to Mineralogy and Petrology, 167, 1025

Boone, M., De Witte, Y., Dierick, M., Almeida, A., and Van Hoorebeke, L. (2012) Improved signal-to-noise ratio in laboratory-based phase contrast tomography. Microscopy and Microanalysis: The Official Journal of Microscopy Society of America, Microbeam Analysis Society, Microscopical Society of Canada, 18, 399–405.

Breiman, L. (2001) Random forests. In R.E. Schapire, Ed., Machine Learning, pp. 5–32. Kluwer Academic Publishers.

Buades, A., Coll, B., and Morel, J.M. (2005) A non-local algorithm for image denoising. In Proceedings—2005 IEEE Computer Society Conference on Computer Vision and Pattern Recognition, CVPR 2005 Vol. II, pp. 60–65.

Chamberlain, K.J., Morgan, D.J., and Wilson, C.J.N. (2014) Timescales of mixing and mobilisation in the Bishop Tuff magma body: Perspectives from diffusion chronometry. Contributions to Mineralogy and Petrology, 168.

Chambers, M., Memeti, V., Eddy, M.P., and Schoene, B. (2020) Half a million years of magmatic history recorded in a K-feldspar megacryst of the Tuolumne Intrusive Complex, California, U.S.A. Geology, 48, 400–404.

Chantler, C.T. (2000) detailed tabulation of atomic form factors, photoelectric absorption and scattering cross section, and mass attenuation coefficients in the vicinity of absorption edges in the soft X-ray (Z = 30–36, Z = 60–89, E = 0.1 keV–10 keV), addressing convergence issues of. Journal of Physical and Chemical Reference Data, 29, 597–1056.

Cnudde, V., and Boone, M.N. (2013) High-resolution X-ray computed tomography in geosciences: A review of the current technology and applications. Earth-Science Reviews, 123, 1–17.

Cooper, K.M. (2017) What does a magma reservoir look like? the "crystal's-eye" view. Elements, 13, 23–28.

Cooper, K.M., and Kent, A.J.R. (2014) Rapid remobilization of magmatic crystals kept in cold storage. Nature, 506, 480–483.

Costa, F., and Dungan, M. (2005) Short time scales of magmatic assimilation from diffusion modeling of multiple elements in olivine. Geology, 33, 837–840.

Costa, F., Chakraborty, S., and Dohmen, R. (2003) Diffusion coupling between major and trace elements and a model for the calculation of magma chamber residence times using plagioclase. Geochimica et Cosmochimica Acta, 67, 2189–2200

Couperthwaite, F.K., Morgan, D.J., Pankhurst, M.J., Lee, P.D., and Day, J.M.D. (2021) Reducing epistemic and model uncertainty in ionic inter-diffusion chronology: A 3D observation and dynamic modeling approach using olivine from Piton de la Fournaise, la Réunion. American Mineralogist, 106, 481–494.

Davidson, J.P., and Tepley, F.J. (1997) Recharge in Volcanic Systems: Evidence from Isotope Profiles of Phenocrysts. Science, 275, 826–829.

- Davidson, J., Tepley, F., Palacz, Z., and Meffan-Main, S. (2001) Magma recharge, contamination and residence times revealed by in situ laser ablation isotopic analysis of feldspar in volcanic rocks. Earth and Planetary Science Letters, 184. 427–442.
- de Silva, S.L., and Gregg, P.M. (2014) Thermomechanical feedbacks in magmatic systems: Implications for growth, longevity, and evolution of large calderaforming magma reservoirs and their supereruptions. Journal of Volcanology and Geothermal Research, 282, 77–91.
- Deer, W.A., Howie, R.A., and Zussman, J. (1966) An Introduction to the Rock-Forming Minerals. Wiley
- Denison, D., Carlson, W.D., and Ketcham, R.A. (1997) Three-dimensional quantitative textural analysis of metamorphic rocks using high-resolution computed X-ray tomography: Part I. Methods and techniques. Journal of Metamorphic Geology, 15, 29–44.
- Eichelberger, J.C. (1975) Origin of andesite and dacite: Evidence of mixing at Glass Mountain in California and at other circum-Pacific volcanoes. Geological Society of America Bulletin, 86, 1381–1391.
- Forni, F., Petricca, E., Bachmann, O., Mollo, S., De Astis, G., and Piochi, M. (2018) The role of magma mixing/mingling and cumulate melting in the Neapolitan Yellow Tuff caldera-forming eruption (Campi Flegrei, Southern Italy). Contributions to Mineralogy and Petrology, 173, 1–18.
- Gelman, S.E., Gutiérrez, F.J., and Bachmann, O. (2013) On the longevity of large upper crustal silicie magma reservoirs. Geology, 41, 759–762.
- Geurts, P., Ernst, D., and Wehenkel, L. (2006) Extremely randomized trees. Machine Learning, 63, 3–42.
- Giachetti, T., Burgisser, A., Arbaret, L., Druitt, T.H., and Kelfoun, K. (2011) Quantitative textural analysis of Vulcanian pyroclasts (Montserrat) using multi-scale X-ray computed microtomography: Comparison with results from 2D image analysis. Bulletin of Volcanology, 73, 1295–1309.
- Ginibre, C., Wörner, G., and Kronz, A. (2004) Structure and dynamics of the Laacher See magma chamber (Eifel, Germany) from major and trace element zoning in sanidine: A cathodoluminescence and electron microprobe study. Journal of Petrology, 45, 2197–2223.
- Gualda, G.A.R., and Rivers, M. (2006) Quantitative 3D petrography using X-ray tomography: Application to Bishop Tuff pumice clasts. Journal of Volcanology and Geothermal Research, 154, 48–62.
- Gualda, G.A.R., Pamukcu, A.S., Claiborne, L.L., and Rivers, M.L. (2010) Quantitative 3D petrography using X-ray tomography 3: Documenting accessory phases with differential absorption tomography. Geosphere, 6, 782–792.
- Hanna, R.D., and Ketcham, R.A. (2017) X-ray computed tomography of planetary materials: A primer and review of recent studies. Geochemistry, 77, 547–572.
- Higgins, M.D. (2000) Measurement of crystal size distributions. American Mineralogist, 85, 1105–1116.
- Icenhower, J., and London, D. (1996) Experimental partitioning of Rb, Cs, Sr and Ba between alkali feldspar and peraluminous melt. American Mineralogist, 81, 719–734.
- Jähne, B., Haußecker, H., and Geißler, P. (1999) 3D computer vision and applications. Proceedings—International Conference on Pattern Recognition Vol. 1.
- Kent, A.J.R., Darr, C., Koleszar, A.M., Salisbury, M.J., and Cooper, K.M. (2010) Preferential eruption of andesitic magmas through recharge filtering. Nature Geoscience, 3, 631–636.
- Krimer, D., and Costa, F. (2017) Evaluation of the effects of 3D diffusion, crystal geometry, and initial conditions on retrieved time-scales from Fe-Mg zoning in natural oriented orthopyroxene crystals. Geochimica et Cosmochimica Acta, 196, 271–288.
- Lipman, P.W., and McIntosh, W.C. (2008) Eruptive and noneruptive calderas, northeastern San Juan Mountains, Colorado: Where did the ignimbrites come from? Geological Society of America Bulletin, 120, 771–795.
- Lubbers, J., Deering, C., and Bachmann, O. (2020) Genesis of rhyolitic melts in the upper crust: Fractionation and remobilization of an intermediate cumulate at Lake City caldera, Colorado, U.S.A. Journal of Volcanology and Geothermal Research, 392, 106750.
- Matthews, N.E., Vazquez, J.A., and Calvert, C.T. (2015) Age of the Lava Creek supereruption and magma chamber assembly at Yellowstone based on <sup>40</sup>Ar/<sup>39</sup>Ar and U-Pb dating of sanidine and zircon crystals. Geochemistry, Geophysics, Geosystems, 16, 2508–2528.
- McCullough, E.C. (1975) Photon attenuation in computed tomography. Medical Physics, 2, 307–320.
- McIntire, W.L. (1963) Trace element partition coefficients—a review of theory and applications to geology. Geochimica et Cosmochimica Acta, 27, 1209–1264.
- Morgan, D.J., and Blake, S. (2006) Magmatic residence times of zoned phenocrysts: Introduction and application of the binary element diffusion modelling (BEDM) technique. Contributions to Mineralogy and Petrology, 151, 58–70.
- Mourey, A.J., and Shea, T. (2019) Forming olivine phenocrysts in basalt: A 3D characterization of growth rates in laboratory experiments. Frontiers in Earth Science, 7, 1–16.
- Pamukcu, A.S., and Gualda, G.A.R. (2010) Quantitative 3D petrography using X-ray tomography 2: Combining information at various resolutions. Geosphere, 6, 775–781.

- Pankhurst, M.J., Dobson, K.J., Morgan, D.J., Loughlin, S.C., Thordarson, T.H., Lee, P.D., and Courtois, L. (2014) Monitoring the magmas fuelling volcanic eruptions in near-real-time using X-ray micro-computed tomography. Journal of Petrology, 55, 671–684.
- Pankhurst, M.J., Vo, N.T., Butcher, A.R., Long, H., Wang, H., Nonni, S., Harvey, J., Gudfinnsson, G., Fowler, R., Atwood, R., Walshaw, R., and Lee, P.D. (2018) Quantitative measurement of olivine composition in three dimensions using helical-scan X-ray micro-tomography. American Mineralogist, 103, 1800–1811.
- Pankhurst, M.J., Gueninchault, N., Andrew, M., and Hill, E. (2019) Non-destructive three-dimensional crystallographic orientation analysis of olivine using laboratory diffraction contrast tomography. Mineralogical Magazine, 83, 705–711.
- Pedregosa, F., Varoquaux, G., Alexandre, G., Michel, V., Thirion, B., Grisel, O., Blondel, M., Prettenhofer, P., Weiss, R., Dubourg, V. and others (2011) Scikitlearn: Machine learning in Python. Journal of Machine Learning Research, 12, 2825–2830.
- Petrelli, M., Caricchi, L., and Perugini, D. (2020) Machine learning thermo-barometry: Application to clinopyroxene-bearing magmas. Journal of Geophysical Research: Solid Earth, 125.
- Reddy, S.M., Saxey, D.W., Rickard, W.D.A., Fougerouse, D., Montalvo, S.D., Verberne, R., and Riessen, A. (2020) Atom probe tomography: Development and application to the geosciences. Geostandards and Geoanalytical Research. 44, 5–50.
- Rickard, W.D.A., Reddy, S.M., Saxey, D.W., Fougerouse, D., Timms, N.E., Daly, L., Peterman, E., Cavosie, A.J., and Jourdan, F. (2020) Novel applications of FIB-SEM-Based ToF-SIMS in atom probe tomography workflows. Microscopy and Microanalysis, 26, 750–757.
- Roerdink, J.B.T.M., and Meijster, A. (2000) The watershed transform: definitions, algorithms and parallelization strategies. Fundamenta Informaticae, 41, 187–228.
- Rout, S.S., Blum-Oeste, M., and Wörner, G. (2021) Long-term temperature cycling in a shallow magma reservoir: Insights from sanidine megacrysts at Taápaca volcano, Central Andes ABSTRACT. Journal of Petrology, 62.
- Rubin, A.E., Cooper, K.M., Till, C.B., Kent, A.J.R., Costa, F., Bose, M., Gravley, D., Deering, C., and Cole, J. (2017) Rapid cooling and cold storage in a silicic magma reservoir recorded in Individual Crystals. Science, 356, 1154–1156.
- Ruprecht, P., and Plank, T. (2013) Feeding andesitic eruptions with a high-speed connection from the mantle. Nature, 500, 68–72.
- Schneider, C.A., Rasband, W.S., and Eliceiri, K.W. (2012) NIH Image to ImageJ: 25 years of image analysis. Nature Methods, 9, 671–675.
- Shamloo, H.I., and Till, C.B. (2019) Decadal transition from quiescence to supereruption: petrologic investigation of the Lava Creek Tuff, Yellowstone Caldera, WY. Contributions to Mineralogy and Petrology, 174, 1–18.
- Shea, T., Costa, F., Krimer, D., and Hammer, J.E. (2015) Accuracy of timescales retrieved from diffusion modeling in olivine: A 3D perspective. American Mineralogist, 100, 2026–2042.
- Sheppard, A., Latham, S., Middleton, J., Kingston, A., Myers, G., Varslot, T., Fogden, A., Sawkins, T., Cruikshank, R., Saadatfar, M., and others. (2014) Techniques in helical scanning, dynamic imaging and image segmentation for improved quantitative analysis with X-ray micro-CT. Nuclear Instruments and Methods in Physics Research Section B: Beam Interactions with Materials and Atoms, 324, 49–56.
- Simonetti, A., Shore, M., and Bell, K. (1996) Diopside phenocrysts from nephelinite lavas, Napak volcano, eastern Uganda: Evidence for magma mixing. Canadian Mineralogist, 34, 411–421.
- Singer, B.S., Dungan, M.A., and Layne, G.D. (1995) Textures and Sr, Ba, Mg, Fe, K, and Ti compositional profiles in volcanic plagioclase: Clues to the dynamics of calc-alkaline magma chambers. American Mineralogist, 80, 776–798.
- Spear, F.S., and Daniel, C.G. (2003) Three-dimensional imaging of garnet porphyroblast sizes and chemical zoning: Nucleation and growth history in the garnet zone. American Mineralogist, 88, 245.
- Streck, M.J., Dungan, M.A., Bussy, F., and Malavassi, E. (2005) Mineral inventory of continuously erupting basaltic andesites at Arenal volcano, Costa Rica: Implications for interpreting monotonous, crystal-rich, mafic arc stratigraphies. Journal of Volcanology and Geothermal Research, 140, 133–155.
- Szymanowski, D., Wotzlaw, J.-F., Ellis, B.S., Bachmann, O., Guillong, M., and von Quadt, A. (2017) Protracted near-solidus storage and pre-eruptive rejuvenation of large magma reservoirs. Nature Geoscience, 10, 777–782.
- Szymanowski, D., Ellis, B.S., Wotzlaw, J.-F., and Bachmann, O. (2019) Maturation and rejuvenation of a silicic magma reservoir: High-resolution chronology of the Kneeling Nun Tuff. Earth and Planetary Science Letters, 510, 103–115.
- Tajčmanová, L., Abart, R., Wirth, R., Habler, G., and Rhede, D. (2012) Intracrystal-line microstructures in alkali feldspars from fluid-deficient felsic granulites: A mineral chemical and TEM study. Contributions to Mineralogy and Petrology, 164, 715–729.
- Tepley, F.J., Davidson, J.P., Tilling, R.I., and Arth, J.G. (2000) Magma mixing, recharge, and eruption histories recorded in plagioclase phenocrysts from El Chichon Volcano, Mexico. Journal of Petrology, 41, 1397–1411.
- Till, C.B., Vazquez, J.A., and Boyce, J.W. (2015) Months between rejuvenation and

- volcanic eruption at Yellowstone caldera, Wyoming. Geology, 43, 695–698. Tsuchiyama, A., Nakano, T., Uesugi, K., Uesugi, M., Takeuchi, A., Suzuki, Y., Noguchi, R., Matsumoto, T., Matsuno, J., Nagano, T., and others. (2013) Analytical dual-energy microtomography: A new method for obtaining three-dimensional mineral phase images and its application to Hayabusa samples. Geochimica et Cosmochimica Acta, 116, 5–16.
- Uesugi, M., Uesugi, K., and Oka, M. (2010) Non-destructive observation of meteorite chips using quantitative analysis of optimized X-ray micro-computed tomography. Earth and Planetary Science Letters, 299, 359–367.
- Van Der Walt, S., Schönberger, J.L., Nunez-Iglesias, J., Boulogne, F., Warner, J.D., Yager, N., Gouillart, E., and Yu, T. (2014) Scikit-image: Image processing in python. PeerJ, 2, e453
- Van Grieken, R., and Markowicz, A. (2002) Handbook of X-ray Spectrometry, 2nd ed. Marcel Dekker.
- Varslot, T., Kingston, A., Sheppard, A., and Sakellariou, A. (2011a) Fast highresolution micro-CT with exact reconstruction methods. Developments in X-Ray Tomography VII, 7804, 780413.
- Varslot, T., Kingston, A., Myers, G., and Sheppard, A. (2011b) High-resolution helical cone-beam micro-CT with theoretically-exact reconstruction from experimental data. Medical Physics, 38, 5459–5476.
- Vincent, L., and Soille, P. (1991) Watersheds in digital spaces: An efficient algorithm based on immersion simulations. IEEE Transactions on Pattern Analysis and Machine Intelligence, 13, 583–598.
- Voltolini, M., Zandomeneghi, D., Mancini, L., and Polacci, M. (2011) Texture analysis of volcanic rock samples: Quantitative study of crystals and vesicles shape preferred orientation from X-ray microtomography data. Journal of Volcanology and Geothermal Research, 202, 83–95.
- Wildenschild, D., and Sheppard, A.P. (2013) X-ray imaging and analysis techniques for quantifying pore-scale structure and processes in subsurface porous medium systems. Advances in Water Resources, 51, 217–246.
- Willmott, P. (2011) An Introduction to Synchrotron Radiation. Wiley

- Wirth, R. (2009) Focused Ion Beam (FIB) combined with SEM and TEM: Advanced analytical tools for studies of chemical composition, microstructure and crystal structure in geomaterials on a nanometre scale. Chemical Geology, 261, 217–229.
- Wolff, J.A., Ellis, B.S., Ramos, F.C., Starkel, W.A., Boroughs, S., Olin, P.H., and Bachmann, O. (2015) Remelting of cumulates as a process for producing chemical zoning in silicic tuffs: A comparison of cool, wet and hot, dry rhyolitic magma systems. Lithos, 236-237, 275–286.
- Wolff, J.A., Forni, F., Ellis, B.S., and Szymanowski, D. (2020) Europium and barium enrichments in compositionally zoned felsic tuffs: A smoking gun for the origin of chemical and physical gradients by cumulate melting. Earth and Planetary Science Letters, 540, 116251.
- Zandomeneghi, D., Voltolini, M., Mancini, L., Brun, F., Dreossi, D., and Polacci, M. (2010) Quantitative analysis of X-ray microtomography images of geomaterials: Application to volcanic rocks. Geosphere, 6, 793–804.
- Zhang, Y. (2010) Diffusion in minerals and melts: Theoretical background. Reviews in Mineralogy and Geochemistry, 72, 5–59.

Manuscript received May 17, 2021
Manuscript accepted January 30, 2022
Accepted manuscript online February 10, 2022
Manuscript handled by Maurizio Petrelli

#### **Endnote:**

<sup>1</sup>Deposit item AM-23-28139, Online Materials. Deposit items are free to all readers and found on the MSA website, via the specific issue's Table of Contents (go to http://www.minsocam.org/MSA/AmMin/TOC/2023/Feb2023\_data/Feb2023\_data.html).